Research Square

Preprints are preliminary reports that have not undergone peer review.
They should not be considered conclusive, used to inform clinical practice,
or referenced by the media as validated information.

MXRA8 confers respiratory tropism and drives systemic dissemination of Chikungunya virus

Xiang Gao

gaoxiang609@126.com

National Key Laboratory of Advanced Biotechnology https://orcid.org/0009-0009-4372-4627

Lihua Ding

https://orcid.org/0000-0002-5280-8162

Wenting Liu

National Key Laboratory of Advanced Biotechnology

Zhang Zhang

Beijing Institute of Biotechnology

Huiyuan Li

National Key Laboratory of Advanced Biotechnology

Hongtao Duan

National Key Laboratory of Advanced Biotechnology

Hua-Cheng Yan

Southern Medical University

Fangfang He

Lecong Hospital of Shunde Foshan

Cuixiang Yi

Lecong Hospital of Shunde Foshan

Jun Zhang

Beijing Institute of Biotechnology https://orcid.org/0000-0002-9650-112X

Xiaojuan Liu

Peking University Third Hospital

Article

Keywords:

Posted Date: March 27th, 2026

DOI: https://doi.org/10.21203/rs.3.rs-8887327/v1

License: This work is licensed under a Creative Commons Attribution 4.0 International License.
Read Full License

Additional Declarations: There is **NO** Competing Interest.

MXRA8 confers respiratory tropism and drives systemic dissemination of Chikungunya virus

Lihua Ding[1,5], Wenting Liu[1,5], Zhang Zhang[1,5], Huiyuan Li[1], Hongtao Duan[1], Huacheng Yan[3], Fangfang He[4], Cuixiang Yi[4], Jun Zhang[1✉], Xiaojuan Liu[2✉], Xiang Gao[1✉]

[1]National Key Laboratory of Advanced Biotechnology, Beijing, China.

[2]Peking University Third Hospital, Beijing, China.

[3]Southern China Center for Disease Control and Prevention, Guangzhou, China.

[4]Lecong Hospital of Shunde Foshan, Foshan, Guangdong, China.

[5]These authors contributed equally: Lihua Ding, Wenting Liu, Zhang Zhang.

✉e-mail: justforhere@126.com; liuxiaojuanjuan@126.com; gaoxiang609@126.com

Abstract

Chikungunya virus (CHIKV) is a re-emerging alphavirus causing explosive urban outbreaks worldwide. Historically, its pathogenesis has been restricted to a canonical mosquito-host cycle wherein cutaneous inoculation drives systemic inflammation. However, the biological mechanisms sustaining its rapid transmission dynamics remain incompletely defined. Here, we identify the human respiratory tract as a highly permissive amplification niche. Patient nasopharyngeal swabs reveal high viral loads, while human nasal and airway organoids demonstrate robust replication and bidirectional release facilitating respiratory shedding and systemic dissemination. Single-nucleus RNA sequencing (snRNA-seq) delineates a pan-epithelial infection landscape, revealing a transcriptional reprogramming that drives pro-inflammatory signaling while simultaneously suppressing homeostatic tissue repair. Mechanistically, CHIKV engages the Matrix Remodeling Associated 8 (MXRA8) receptor for entry and exploits tunneling nanotubes (TNTs) for covert spread. In AG129 mice, intranasal inoculation triggers necrotizing respiratory cytopathology, breaching the mucosal barrier to seed systemic infection. This reveals a pathogenic dichotomy where airway necrosis contrasts with the characteristic inflammatory storm in distal musculoskeletal targets. Collectively, these findings establish an MXRA8-mediated arbo-respiratory axis, identifying the respiratory mucosa as a previously overlooked reservoir that critically enhances systemic pathogenesis and transmission efficiency.

Introduction

Chikungunya virus (CHIKV) is a re-emerging arthritogenic alphavirus responsible for debilitating acute febrile illness and chronic polyarthralgia worldwide[1-4]. Since its discovery in 1952, CHIKV has caused massive epidemics across Africa, Asia, Europe, and the Americas, imposing a severe public health burden[5-8]. Historically, the understanding of CHIKV pathogenesis has been strictly defined by a canonical mosquito-host cycle, wherein transmission via Aedes bites drives local replication and subsequent hematogenous dissemination to musculoskeletal tissues[2,9,10]. While this model explains basal transmission dynamics, it fails to fully account for rapid transmission kinetics of high-density urban outbreaks, where attack rates frequently exceed 30-75% within weeks[11-13]. The emergence of viral strains with enhanced vector adaptability, such as the E1-A226V mutation, partially explains this efficiency but does not fully resolve the rapid dissemination observed in non-vector optimal conditions[14]. Furthermore, vector-centric frameworks do not resolve the mechanisms driving the severe systemic inflammation and atypical manifestations, including encephalitis, myocarditis, and multi-organ failure, which have been observed in a significant subset of patients[15,16].

Although CHIKV is not canonically classified as a respiratory pathogen, severe infections observed in neonates, the elderly, and individuals with comorbidities are increasingly associated with atypical complications and fatal outcomes[12,17-19]. While recent autopsy studies have detected viral RNA in the lungs of fatal cases, the presence of viral antigens in lung tissue has historically been attributed to passive vascular leakage or systemic congestion rather than active mucosal replication[9,20]. Consequently, the potential for arboviruses to leverage respiratory niches remains a critical yet under-investigated frontier in viral pathogenesis[21,22]. Unlike classical respiratory viruses such as influenza and coronaviruses that utilize the airway as a primary portal of entry and replication[2,23], the role of the respiratory tract in driving arboviral dissemination is poorly understood. Defining the capacity of CHIKV to productively infect airway tissues and elucidating the molecular mechanisms governing this tropism are therefore essential for constructing a complete model of

early viral spread and systemic inflammation[24]. Crucially, while the cognate receptor Matrix Remodeling Associated 8 (MXRA8) is well-documented to govern viral tropism in skin and musculoskeletal tissues, its expression landscape and potential function within the human respiratory mucosa remain entirely unknown[25,26].

Here, we identify the human respiratory tract as a highly permissive reservoir for CHIKV that functions as a cryptic replicative niche, evidenced by high viral RNA loads detected in patient nasopharyngeal swabs and robust replication observed in human airway organoids. Single-nucleus RNA sequencing (snRNA-seq) further delineates a pan-epithelial infection landscape, revealing a virus-induced transcriptional reprogramming that activates pro-inflammatory signaling while suppressing homeostatic tissue repair. Mechanistically, we demonstrate that CHIKV engages the apically expressed MXRA8 receptor for entry and exploits tunneling nanotubes (TNTs) for covert intercellular dissemination, thereby evading extracellular antibody neutralization[25,27-31]. In the AG129 mouse model, this respiratory infection drives necrotizing cytopathology that breaches the mucosal barrier to seed distal joints and muscles[32,33]. Finally, we delineate a distinct pathogenic dichotomy wherein the respiratory tract undergoes necrotizing cytopathology to propel systemic dissemination while the musculoskeletal targets mount a characteristic inflammatory storm[20,34,35]. These findings reveal a previously unrecognized arbo-respiratory axis that operates in parallel with the vector-borne cycle to critically enhance systemic pathogenesis.

Results

The human respiratory tract is a permissive reservoir for CHIKV amplification and bidirectional release

To investigate the respiratory tract as a potential site for viral amplification, we analyzed nasopharyngeal swabs from a clinical cohort of systemically infected patients (n = 26; Supplementary Table 1). High-titer viral RNA was recovered from the upper airway of most CHIKV-positive individuals (reaching 10^6 copies/ml), whereas specificity controls (including the Zika-infected Patient-23; Supplementary

Table 1) and negative controls remained below the limit of detection (Fig. 1a and Extended Data Fig. 1a). To dissect the cellular determinants of this intrinsic susceptibility, we established respiratory organoids derived from nasopharyngeal swabs (nasal) and resected lung tissue (airway). These models faithfully recapitulated native mucociliary architecture, evidenced by the presence of mature motile cilia[36,37] (Extended Data Fig. 2a-c) and the physiological distribution of β-tubulin^{+} ciliated cells, MUC5AC^{+} goblet cells, CC10^{+} club cells, and p63^{+} basal progenitors (Extended Data Fig. 2d).

Inoculation of these validated physiological models demonstrated robust, exponential viral replication following either apical or basolateral challenge (Fig. 1b,c). Crucially, infectious progeny were secreted bidirectionally (Fig. 1d,e), suggesting that the respiratory mucosa functions as a dual-action interface that facilitates environmental transmission via apical shedding while simultaneously driving systemic dissemination through basolateral egress. To exclude passive paracellular leakage as a cause of this bipolar secretion, we assessed epithelial barrier integrity. High transepithelial electrical resistance (TEER) values confirmed the maintenance of a tight physiological seal (Extended Data Fig. 2e), indicating that the observed release kinetics were governed by active viral egress rather than barrier defects. Ultrastructural analysis substantiated this productive infection, revealing dense virion clusters within cytoplasmic cytopathic vacuoles (CPVs), a hallmark of alphavirus replication factories (Fig. 1f). Notably, we observed active viral budding at the plasma membrane and the formation of tunneling nanotubes (TNTs) bridging adjacent cells (Fig. 1g), identifying a potential mechanism for efficient intercellular spread. Collectively, these data establish the respiratory mucosa as a *bona fide* target organ where efficient replication and bidirectional release converge to drive the rapid viremic kinetics characteristic of acute CHIKV infection.

CHIKV targets diverse epithelial lineages and disrupts junctional integrity

To elucidate the cellular tropism sustaining mucosal amplification, we performed high-resolution immunofluorescence mapping against lineage-specific markers. In

both nasal and airway organoids, CHIKV exhibited a broad, pan-epithelial infection profile consistent with productive replication in diverse cell types (Fig. 2a, b). The virus productively targeted differentiated luminal cells, including multiciliated (β-tubulin^{+}) and secretory lineages, comprising goblet (MUC5AC^{+}) and club cells (CC10^{+}). Crucially, basal progenitors (p63^{+}) were also susceptible, indicating that the regenerative compartment is compromised. CHIKV infection significantly promoted MUC5AC expression within infected foci, indicative of virus-induced mucin hypersecretion (Fig. 2a, b).

As the respiratory epithelium functions as a primary physical barrier, we next investigated the integrity of tight junctions. In mock-infected controls, Zonula Occludens-1 (ZO-1) formed a continuous polygonal lattice that outlined the apical cell borders. In contrast, CHIKV infection provoked severe disassembly of these junctional complexes (Fig. 2c, d). We observed fragmentation, discontinuity, and cytosolic delocalization of ZO-1 in E2-positive regions. This widespread dissolution of the apical junctional seal provides a mechanistic explanation for the loss of barrier function. Collectively, these data reveal that CHIKV overcomes respiratory defenses by coupling broad cellular tropism with the targeted disintegration of epithelial integrity, effectively converting the mucosa from a protective barrier into a gateway for systemic invasion.

Single-cell profiling reveals a pan-epithelial antiviral lockdown and disrupted homeostatic circuitry

To delineate the transcriptomic landscape of CHIKV-infected respiratory mucosa without the dissociation bias inherent to fragile infected tissues, we employed single-nucleus RNA sequencing (snRNA-seq) to capture the nascent nuclear transcriptome (Fig. 3a). Unbiased clustering successfully identified five distinct epithelial lineages comprising Basal, Parabasal, Secretory, Pre-ciliated, and Ciliated cells that faithfully recapitulated the physiological airway architecture[38]. The molecular identity of these clusters was defined by the enrichment of canonical lineage markers such as TP63 (p63) for basal progenitors and FOXJ1 for ciliated cells

(Fig. 3b, c; Extended Data Fig. 4a).

Differential expression analysis revealed a profound transcriptional reprogramming across all lineages (Fig. 3d). We observed a massive upregulation of interferon-stimulated genes (ISGs), including BST2, PTGS2, NFKB1A, and IFNGR1, that reflected a coordinated antiviral state aimed at restricting viral replication[39,40]. Concurrently, a subset of homeostatic genes was downregulated and underscored a strategic metabolic shift from maintenance to defense. Pathway enrichment analysis resolved cell-type-specific nuances in this response where pre-ciliated cells primarily enriched Interferon-α/β signaling and Cytokine signaling (Fig. 3e), while secretory epithelial cells emerged as a pro-inflammatory hub characterized by the enrichment of NOD-like receptor signaling, TNF signaling, and IL-17 signaling pathways (Fig. 3f). This suggests that secretory lineages may function as sentinel sensors that initiate the inflammatory cascade.

Quantification of antiviral states revealed a stratified response landscape rather than a uniform induction across the epithelium (Fig. 3g), characterized by robust defenses in Parabasal and Secretory lineages that contrasted with muted activity in Basal and Ciliated cells. Heatmap analysis further resolved this functional heterogeneity by uncovering lineage-specific effector programs where Secretory cells preferentially deployed CXCL10 and PTGS2, while Ciliated cells upregulated HLA class II genes, suggestive of coordinated antigen presentation and chemotaxis (Fig. 3h). Crucially, we validated these transcriptomic signatures in nasal organoids via qPCR and confirmed the robust induction of Type III interferons (IFNL1/2/3), pro-apoptotic markers (BAX), and key ISGs (MX1, OAS1) (Fig. 3i, Supplementary Table 2) to corroborate the gene expression changes observed by single-nucleus profiling[41].

To determine if this potent antiviral programming compromises tissue integrity, we reconstructed intercellular communication networks using CellChat (Extended Data Fig. 4b). Visualizing global signaling patterns revealed a dramatic topological rewiring of ligand-receptor interactions upon infection. Analysis of information flow exposed a functional collapse of canonical maintenance modules where signaling via EGF, WNT, NOTCH, and LAMININ pathways essential for epithelial renewal and

basal membrane anchorage was severely abrogated or lost (Extended Data Fig. 4c). Conversely, the tissue prioritized stress-response networks dominated by a surge in Midkine (MK), TGF-β, and SEMA4 signaling (Extended Data Fig. 4c). This disruption of intercellular homeostasis was paralleled by intracellular perturbations in which ciliated cells enriched pathways associated with DNA damage and compromised cell-extracellular matrix interactions while parabasal progenitors exhibited signs of metabolic stress and aberrant keratinization (Extended Data Fig. 4d). This diametric shift uncovers a pathogenic trade-off where the respiratory mucosa orchestrates a comprehensive antiviral lockdown that inadvertently suppresses stem cell maintenance and repair circuitry to provide a transcriptional mechanism for the observed epithelial disintegration. Taken together, these analyses provide a comprehensive molecular framework for CHIKV respiratory pathogenesis and identify the specific uncoupling of maintenance signaling amidst a heterogeneous antiviral landscape as the primary driver of the necrotizing barrier breach.

Intranasal CHIKV challenge drives severe respiratory cytopathology and systemic dissemination

To validate the respiratory tract as a productive portal of entry *in vivo*, we challenged highly susceptible type I/II interferon receptor-deficient mice (AG129) via the intranasal route (Fig. 4a)[32]. Longitudinal monitoring confirmed productive mucosal replication that was evidenced by the detection of significant viral RNA loads in nasal washes at 3 and 7 days post-infection (d.p.i.) (Extended Data Fig. 5a). To assess systemic dissemination, we quantified viral burden in terminal tissues (10 d.p.i.). The results revealed that the lungs harbored the highest viral loads while significant viral RNA levels were consistently detected in the nasal turbinates, blood, joints, and muscles (Fig. 4b). Despite this widespread viral seeding, histopathological analysis revealed a striking divergence in tissue damage. The nasal turbinates exhibited extensive necrosis, epithelial sloughing, and hemorrhage while the lungs displayed features of severe interstitial pneumonia including alveolar septal thickening and collapse (Fig. 4c). In contrast, the classical musculoskeletal target

tissues comprising joints and muscles maintained a relatively preserved histological architecture without overt myositis or arthritis (Fig. 4c). Immunofluorescence staining detected abundant viral E2 antigen colocalizing with the MXRA8 receptor within the nasal and pulmonary mucosa as well as within the myofibers, proving that the virus successfully breached the respiratory barrier to seed systemic sites. However, distinct E2 staining was absent in articular tissues, likely due to epitope loss during the decalcification of osseous tissues (Fig. 4d). Transcriptional profiling unveiled a striking tissue-specific dichotomy in immune activation. While the respiratory tract succumbing to direct viral cytolysis mounted a specific mucosal response characterized by Ifi27 and Type III interferons (Ifnl2/3), the structurally intact musculoskeletal tissues were already in the throes of a molecular cytokine storm. The joints and muscles exhibited a hyper-inflammatory signature with profound upregulation of Il6, Mx1, and Isg15 (Fig. 4e). Together, these data demonstrate that intranasal CHIKV exposure leads to rapid respiratory amplification and systemic spread in which direct viral cytopathology drives mucosal injury while disseminated virus triggers a potent pre-lesional inflammatory cascade in musculoskeletal tissues.

MXRA8 is the essential entry receptor for CHIKV in human respiratory epithelium

To delineate the molecular mechanism governing respiratory tropism, we investigated the role of Matrix Remodeling Associated 8 (MXRA8), the cognate receptor for arthritogenic alphaviruses[25,27]. Immunofluorescence staining of clinical lung biopsies confirmed the physiological presence of MXRA8 in human pulmonary tissue (Fig. 5a and Supplementary Table 3). To rigorously validate receptor availability in our *in vitro* models, we profiled expression levels utilizing HEK293T negative and U2OS positive cell lines as defined reference standards. Consistent with the permissive U2OS control, both confocal microscopy and western blotting revealed robust constitutive MXRA8 expression in nasal and airway organoids while no signal was detected in the HEK293T negative control (Fig. 5b, c). To demonstrate functional causality, we engineered a lentiviral shRNA system to knock down endogenous MXRA8, followed

by complementation with an shRNA-resistant rescue construct (Fig. 5d). Western blot analysis confirmed significant knockdown exceeding 60% and successful restoration of receptor expression in both organoids (Fig. 5d). Strikingly, silencing of MXRA8 abrogated CHIKV susceptibility and resulted in a profound reduction in both intracellular viral RNA copies by over 4 logs and infectious progeny titers following apical challenge (Fig. 5e). Crucially, ectopic re-expression of MXRA8 fully restored viral replicative fitness to wild-type levels. These data definitively establish MXRA8 as the critical, non-redundant gatekeeper for CHIKV acquisition at the respiratory mucosal interface.

Discussion

Traditional epidemiological models relying solely on vector-host cycles cannot fully account for the rapid transmission dynamics of Chikungunya virus (CHIKV) observed in high-density urban outbreaks[11-13], and the precise drivers of this viremic intensity have remained elusive. Integrating our clinical, single-nucleus, and *in vivo* findings, we propose a comprehensive model of pathogenesis (Fig. 5f) in which the human respiratory tract functions as a cryptic and high-capacity amplification reservoir. This concept is substantiated by our detection of high viral RNA loads in nasopharyngeal swabs from CHIKV patients (Fig. 1a). While MXRA8 is canonically implicated in musculoskeletal pathogenesis[25-27], we demonstrate that its broad expression across the nasal and pulmonary mucosa directs an opportunistic respiratory tropism. Aided by tunneling nanotubes (TNTs) that facilitate stealth dissemination[29,30] (Fig. 1a), the virus effectively breaches the mucosal barrier to seed distal sites in our AG129 mouse model. Our data define a distinct pathogenic dichotomy characterized by a respiratory tract that undergoes necrotizing epithelial shedding to drive systemic dissemination, while the downstream musculoskeletal targets subsequently mount the characteristic inflammatory cascades associated with arthralgia[34,42].

By establishing the respiratory mucosa as an overlooked driver of systemic viremia, these findings fundamentally challenge the paradigm that arboviral pathogenesis is restricted to peripheral replication sites[2,15]. Crucially, the

arbovirus-respiratory axis represents a functional divergence from classic respiratory pathogens. Unlike viruses such as Influenza or SARS-CoV-2 that are evolutionarily optimized for apical shedding and aerosol transmission[2,23], CHIKV exhibits an opportunistic colonization strategy that utilizes the respiratory mucosa not for inter-host transmission but as a high-titer amplification reservoir to drive deep tissue seeding. This explains the dysregulated host response we observed in the nasal cavity (Fig. 4e) where the virus prioritizes immune evasion to maximize "inward" amplification and vector availability over the environmental stability required for respiratory contagion[31].

A critical question remains regarding the origin of this respiratory colonization. While our *in vivo* models utilized direct intranasal inoculation to establish intrinsic tissue susceptibility, our *ex vivo* organoid data strongly implicate a hematogenous route as the primary driver in natural infection. The robust viral replication observed following basolateral infection demonstrates that CHIKV can efficiently breach the endothelial-epithelial barrier from the systemic circulation, a dissemination strategy that is consistent with its known capacity to infiltrate other privileged sites[20]. This supports a blood-to-airway trajectory in which the high-titer viremia characteristic of the acute phase seeds the respiratory epithelium. However, the precise mechanisms governing viral transmigration across this barrier remain to be fully elucidated. Determining the relative contribution of hematogenous seeding versus direct mucosal entry will require additional *in vivo* studies potentially utilizing intravenous challenge or endothelial-specific receptor ablation to dissect this trajectory.

A significant paradox persists regarding the inability of CHIKV to establish sustained respiratory transmission in humans despite high nasal viral loads. This discrepancy likely reflects specific biological bottlenecks described in comparative viral models[43]. First, the CHIKV lipid envelope is evolutionarily adapted for arthropod vectors and may exhibit insufficient environmental stability for long-range airborne survival compared to respiratory pathogens[3,44]. Second, the necrotizing pathology we observed favors debris-associated shedding that entraps virions within mucus matrices rather than facilitating the expulsion of fine aerosols. This mechanism

likely restricts the aerodynamic range to close-contact droplets rather than true aerosols[45,46. To] rigorously define the boundaries of this transmission potential, future controlled aerosol experiments are required to quantify the environmental stability and infectivity of respiratory-shed virions.

In interpreting our findings, several limitations warrant consideration. Although our use of snRNA-seq successfully circumvented the dissociation bias inherent to fragile infected tissues, the lack of cytoplasmic RNA capture may limit the sensitivity for certain low-abundance transcripts. Additionally, while the AG129 model was essential for recapitulating severe pathology, the systemic absence of interferon signaling may exaggerate dissemination kinetics[32,33]. Nonetheless, the high concordance between our *in vivo* pathology and human organoid dynamics supports the physiological relevance of our conclusions.

Ultimately, recognizing the respiratory tract as both an anatomical sanctuary and a diagnostic window warrants a paradigm shift in global surveillance strategies and necessitates the integration of respiratory testing into the management of emerging arboviral outbreaks. Overall, our findings unveil a cryptic arbo-respiratory life cycle wherein the airway mucosa functions not as a passive barrier but as a high-capacity amplification tower that fundamentally reshapes our understanding of how vector-borne viruses achieve explosive systemic dissemination.

Data availability

Raw data supporting the western blot results (Fig. 5c, d), viral load quantification, infectious titers, and qRT-PCR analyses are provided with this paper as Source Data. All other data are available from the corresponding author upon reasonable request.

Author contributions

X.G., L.D., X.L., and J.Z. conceived and designed the study. W.L. and L.D. performed the *in vitro* and organoid experiments. Z.Z. conducted the animal experiments. H.L. prepared the viral stocks. H.Y., F.H., and C.Y. coordinated clinical specimen collection. L.D., W.L., H.D., and X.G. analyzed the data. The manuscript was written by X.G., L.D., X.L., and J.Z. and reviewed by all authors.

Acknowledgements

We thank Jianmin Li for providing the CHIKV strain. This work was supported by the National Science and Technology Major Project for Prevention and Control of Emerging and Major Infectious Diseases (grant 2025ZD01901100) and the National Natural Science Foundation of China (grants 82574709 and 82273246).

Methods

Human clinical samples

Twenty-six nasal swab samples from Chikungunya virus (CHIKV) patients used for viral load quantification were obtained from Lecong Hospital of Shunde Foshan following the acquisition of informed consent from patients and approval by the Medical Ethics Committee of Lecong Hospital of Shunde Foshan. Additionally, eight primary lung adenocarcinomas used for MXRA8 receptor detection were collected from Peking University Third Hospital with informed consent and approval from the Institutional Review Committees. All cases used for clinical viral load quantification comprised 21 males and 5 females ranging from 19 to 69 years of age with a mean age of 41.5 years (Supplementary Table 1). Samples were collected from adjacent non-tumor tissues of patients with Lung Adenocarcinoma (LUAD) as detailed in Supplementary Table 3.

Virus strains and infection

All experiments involving infectious Chikungunya virus (CHIKV), utilizing human nasal and airway organoids as well as animal models, were conducted in a Biosafety Level 2 (BSL-2) laboratory under protocols approved by the Institutional Review Board and Ethics Committee of the National Key Laboratory of Advanced Biotechnology.

The CHIKV strain LR2006 was propagated in Vero E6 cells, where viral titers were determined by plaque assay. For organoid infection, fully differentiated ALI cultures were washed with PBS and inoculated with virus diluted to a multiplicity of infection (MOI) of 0.1 or 1 onto the apical or basolateral surface. After 2 hours of adsorption at 37°C, the inoculum was removed and cells were washed three times to remove unbound virus. Fresh medium was added to the basal chamber and cultures were incubated for the indicated time points ranging from 24 to 96 hours post-infection (h.p.i.).

Establishment and differentiation of human nasal organoids

Human nasal organoids were generated from freshly isolated nasal epithelial cells using a protocol adapted from previous studies[47]. Briefly, nasal cells were collected from the nasal turbinate regions using an iClean specimen collection flocked swab. After washing and digestion with 10× TrypLE Select for 5 min at 37°C, the resultant single cells were embedded in 70% Matrigel (Corning, Corning, NY, USA) and seeded into a 24-well culture plate. After solidification, droplets were incubated in airway organoid expansion medium (AOEM) comprising Advanced DMEM/F12 (Gibco, Thermo Fisher Scientific, Waltham, MA, USA) supplemented with N2, B27, R-spondin 1 conditioned medium, 100 ng/ml Noggin, 25 ng/ml FGF7, 100 ng/ml FGF10, 500 nM A83-01, 500 nM SB202190, and 5 μM Y-27632 for the first 3 days at 37°C in a humidified incubator with 5% CO_2. The expansion medium was replenished every other day, and the 3D undifferentiated organoids were passaged every 1 to 2 weeks. For differentiation, 3D organoids were dissociated into single cells using TrypLE Express and seeded onto collagen-IV-coated Transwell inserts at a density of 2 X 10^5 cells per insert. Cultures were maintained in a submerged state until confluence, after which the apical medium was removed to establish an air-liquid interface (ALI). Differentiation was induced using PneumaCult-ALI medium for 21 to 28 days until robust ciliation and mucus secretion were observed.

Establishment and differentiation of human airway organoids

Human airway organoids were generated from lung tissue using a protocol adapted from previous studies[47]. Briefly, fresh tissues were washed with cold PBS containing antibiotics and digested with 2 mg/ml collagenase IV for 60 min at 37 °C. Dissociated epithelial clusters were resuspended in growth factor-reduced Matrigel (Corning, Corning, NY, USA) and seeded into 24-well plates. Organoids were expanded in AOEM comprising Advanced DMEM/F12 supplemented with N2, B27, R-spondin 1 conditioned medium, 100 ng/ml Noggin, 25 ng/ml FGF7, 100 ng/ml FGF10, 500 nM A83-01, 500 nM SB202190, and 5 μM Y-27632 for the first 3 days. For differentiation, viral infection assays, 3D organoids were dissociated into single cells

using TrypLE Express and seeded onto collagen-IV-coated Transwell inserts at a density of 2 X 10^5 cells per insert. Cultures were maintained in a submerged state until confluence, after which the apical medium was removed to establish an air-liquid interface (ALI). Differentiation was induced using PneumaCult-ALI medium for 21 to 28 days until robust ciliation and mucus secretion were observed.

Single-nucleus RNA sequencing

Raw sequencing data were processed using the Cell Ranger pipeline (version 9.0.1, 10x Genomics). Reads were demultiplexed, aligned to the human reference genome (GRCh38-2024-A), and quantified to generate a gene-barcode matrix. Valid cells were distinguished from empty droplets and background noise based on barcode and Unique Molecular Identifier (UMI) validation. Downstream analysis was performed using the Seurat R package (version 5.4.0). Number of detected genes (nFeature > 400), total UMI counts (nCount > 600), and percentage of mitochondrial genes (counts ≤ 4%) were applied to retain high-quality cells. Data of high-quality cells were normalized using the global-scaling method (LogNormalize) with a scale factor of 10,000. The top 2,000 highly variable features were identified. Principal Component Analysis (PCA) was applied to the normalized and scaled data. The top 30 principal components (PCs), selected based on explained variance, were used for subsequent analyses. To correct for batch effects present in the datasets, the datasets were integrated using the Harmony algorithm. For clustering, a Shared Nearest Neighbor (SNN) graph was constructed based on the integrated PCs. Clusters were then identified using the Leiden algorithm (resolution = 1), and visualized using Uniform Manifold Approximation and Projection (UMAP). For cell type annotation and differential expression analysis, cell clusters were manually annotated based on the expression of canonical marker genes derived from the literature and the Human Protein Atlas (HPA) database. Differentially Expressed Genes (DEGs) between clusters were identified using the Wilcoxon Rank Sum test. Significant DEGs were defined as those with a Fold Change (FC) > 1.5 and a False Discovery Rate (FDR) < 0.05. Functional enrichment analyses were conducted using the clusterProfiler

package (version 4.16.0) to characterize the biological significance of the data. We performed over-representation analysis (ORA) on the identified differentially expressed genes (DEGs) and Gene Set Enrichment Analysis (GSEA) on the ranked gene list. These analyses queried the Gene Ontology (GO), Kyoto Encyclopedia of Genes and Genomes (KEGG), and Reactome databases. Terms with an adjusted P-value < 0.05 were considered statistically significant. Single-cell trajectory analysis was performed using Monocle3 (version 1.4.26) to reconstruct developmental lineages and visualize gene expression dynamics along pseudotime. Cellular differentiation potential was evaluated using CytoTRACE2 (version 1.1.0), with higher CytoTRACE scores indicating a higher stemness state. Intercellular communication networks were inferred using CellChat (version 2.2.0). We quantitatively analyzed the communication probability and strength based on the expression of known ligand-receptor pairs to identify significant signaling pathways and interactions between cell groups.

Transmission electron microscopy

Organoids cultured on Transwell inserts were briefly rinsed and fixation was initiated by adding pre-equilibrated electron microscopy fixative at room temperature. Samples were fixed for 5 min under light-protected conditions. The Transwell insert was detached and the cell layer was gently removed using a sterile blade, followed by unidirectional scraping with a sterile cell scraper to avoid repeated scraping. Collected organoids were resuspended in 500 μL fixative and transferred to labeled microcentrifuge tubes. Samples were further fixed at room temperature for 30 min in the dark, then stored and transported at 4 °C without freezing. Fixed samples were transported to Servicebio at 4 °C using ice packs, where samples were processed for transmission electron microscopy (TEM) using standard protocols.

Animal experiments

AG129 mice lacking types I and II interferon receptors were bred and maintained under specific pathogen-free (SPF) conditions. Six-to-eight-week-old mice of mixed

sex were anesthetized with isoflurane and inoculated intranasally with 10^6 PFU/mL of CHIKV in 40 μL of PBS. Mock-infected mice received PBS alone. Clinical signs and weight loss were monitored daily. At indicated time points, mice were euthanized and tissues comprising nasal turbinates, lungs, joints, and skeletal muscle were harvested for viral load quantification and histology. Quantification of viral RNA loads in indicated tissues (Nasal, Lung, Joint, Muscle, Brain, Blood) at 10 days post-infection (d.p.i.). Data are mean ± s.d. (n = 3 mice with established infection). Data were analyzed using an unpaired two-tailed t test. For viral load quantification, animals with no detectable viral RNA in any tissue were considered uninfected and excluded from the statistical analysis of viral burden (2 out of 5 mice in the CHIKV group)

Plasmids, shRNAs, and lentiviruses

The pCMV3-MXRA8-Flag plasmid was obtained from Sino Biological Inc. The lentiviral vector for MXRA8 knockdown was made by cloning corresponding shRNA-resistant MXRA8 (MXRA8-R) shRNA fragments targeting the sequence 5'-CGGGAAAGTCAAAGGGGAA-3' into pSIH-H1-Puro. Lentiviruses were produced by co-transfecting HEK293T cells with recombinant lentiviral vectors and pPACK Packaging Plasmid Mix using Megatran reagent. Forty-eight hours after transfection, viral supernatants were harvested to infect target cells with 8 μg/mL polybrene. For MXRA8 rescue in MXRA8 knockdown cells, cells were infected with lentivirus carrying MXRA8-R for 24 h. For rescue experiments, MXRA8 expression was restored in MXRA8-knockdown organoids by transfecting organoids with pCMV3-MXRA8-Flag that was resistant to the knockdown construct.

Cell transfection

Lipofectamine 3000 reagent (Thermo Fisher Scientific, Waltham, MA, USA) was used for transfections of plasmids. For plasmid transfection, plasmids and Lipofectamine 3000 were diluted in medium without serum. The two solutions were mixed, incubated for 10 min at room temperature, and added to cells.

Immunofluorescence

Organoids cultured on Transwell inserts were fixed and permeabilized. Cells were blocked with FBS for 30 min. The coverslips were then incubated with mouse anti-P63 (AB735, ABCAM), mouse anti-β-tubulin (T7941-2ML, MilliporeSigma), mouse anti-MU5CAC (AB3649, ABCAM), mouse anti-CC10 (RD, MAB4218), mouse anti-ZO-1 (66452-1-Ig, proteintech), rabbit anti-MXRA8 (PA5-63178, Invitrogen), and Rabbit anti-E2 (abinScience, VK572014) at 4°C overnight. Then, horseradish peroxidase (HRP)-conjugated secondary antibodies (ZB-2301, Zhongshan Biotech) were applied at 37°C for 30 min, and immunoreactive cells were visualized with Fluorescein Amplification Reagent (NEL741001KT, Perkin Elmer). Nuclei were counterstained with 4',6-diamidino-2-phenylindole (DAPI). F-actin was stained with Fluor 647-Phalloidin kit (BB-441425-100T, Bestbio). Confocal images were acquired using a Nikon A1 confocal laser scanning microscope (Nikon).

Reverse transcription-quantitative PCR (RT–qPCR)

Total RNA was isolated using TRIzol reagent (Invitrogen) and reverse transcription was performed using a Quantscript RT kit (Tiangen). Real-time quantitative PCR was performed with SYBR green dye on a CFX Opus 96 Real-Time PCR detection system (Bio-Rad). Viral RNA levels were quantified by amplification of the CHIKV E2 gene. Host gene expression was assessed using specific primers for either human or mouse genes, as indicated. Mouse genes included *Gapdh, Ifi27, Mx1, Ifit1, Isg15, Ifitm3, Oas1a, Bst2, Stat1, Socs3, Rplp0, Hprt1, Ppia, Tbp, Il-6, Ifnl2, Ifnl3*, whereas human genes included *MXRA8, GAPDH, PTGS2, MT2A, CYP24A1, IDO1, BAX, BST2, CXCL10, TNF-α, IFNA1, IFNA2, IFNL1, IFNL3, MX1, OAS1, IL-6*, and *IFNL2*. All primer sequences are listed in Supplementary Table 2. The relative quantification value of the target, normalized to mouse *Gapdh* or *GAPDH*, was calculated by the comparative *Ct* method.

Immunoblot analysis

A standard immunoblot was performed. Briefly, cell pellets were lysed in RIPA buffer

containing protease inhibitor on ice for 30 min, and the protein concentration was determined using a BCA protein assay kit (Thermo Fisher Scientific). Equal amounts of protein were subsequently separated by SDS–PAGE and transferred to nitrocellulose membranes. After blocking in 5% skimmed milk for 1 h, membranes were incubated with the rabbit anti-MXRA8 (PA563178, Invitrogen) and rabbit anti-GAPDH (AB0036, Abways) at 4°C overnight or at room temperature for 2 h, followed by incubation with HRP-conjugated IgG at room temperature for 1 h, and then detected by enhanced chemiluminescence. The bands were observed by ChemiDoc Imaging Systems with Image Lab 2.0 software (Bio-Rad).

Multiplex immunofluorescence staining

Multiplex immunofluorescence (mIF) staining of formalin-fixed paraffin-embedded (FFPE) samples was performed as follows. Briefly, formalin-fixed paraffin sections were deparaffinized, rehydrated, and pretreated with 3% H_2O_2 for 20 min to block endogenous peroxidase activity. The antibody-binding epitopes of the antigens were retrieved by microwave treatment, and the sections were then preincubated with 10% goat serum to block nonspecific binding. For double immunofluorescence, rabbit anti-MXRA8 (PA563178, Invitrogen) and rabbit anti-GAPDH (AB0036, Abways) were used as the primary antibodies for IHC. After incubation at 4°C overnight, HRP-conjugated secondary antibodies were applied at 37°C for 1 h. Then, the immunoreactive tissues were stained with Fluorescein Amplification Reagent containing various dyes (FITC, Cy3). After the first fluorescence precipitated, the primary and secondary antibodies were inactivated in citrate buffer (pH 6.0) in a microwave oven. The subsequent fluorescence was then performed as described above. Nuclei were counterstained with 4',6-diamidino-2-phenylindole (DAPI). Confocal images were acquired using a Nikon A1 confocal laser scanning microscope (Nikon).

Hematoxylin and eosin (H&E) staining assay

The formalin-fixed paraffin sections were deparaffinized, rehydrated, and stained with

hematoxylin solution in a staining jar for 10 min. After washing with running water in a staining jar, the sections were stained with eosin solution for 3 min. Then, the sections were successively incubated with 70% ethanol for 20 sec, 90% ethanol for 20 sec, 100% ethanol for 1 min, and xylene for 3 min. The slides were placed in a fume hood and covered with cover slides. Hematoxylin and eosin-stained images were acquired using a KF-PRO-120 automated digital slide scanning system.

Statistical analysis

Statistical analyses were performed using GraphPad Prism Version 10.1.2. Data are presented as mean ± standard error of the mean (SEM) or standard deviation (SD). Differences between the two groups were analyzed using unpaired two-tailed Student's t-test, where a $P < 0.05$ was considered statistically significant.

References

1 Weaver, S. C., Campion, E. W. & Lecuit, M. Chikungunya Virus and the Global Spread of a Mosquito-Borne Disease. *N. Engl. J. Med.* **372**, 1231-1239 (2015).

2 de Souza, W. M., Lecuit, M. & Weaver, S. C. Chikungunya virus and other emerging arthritogenic alphaviruses. *Nat. Rev. Microbiol.* **23**, 585-601 (2025).

3 Silva, L. A. & Dermody, T. S. Chikungunya virus: epidemiology, replication, disease mechanisms, and prospective intervention strategies. *J. Clin. Invest.* **127**, 737-749 (2017).

4 Burt, F. J., Rolph, M. S., Rulli, N. E., Mahalingam, S. & Heise, M. T. Chikungunya: a re-emerging virus. *Lancet* **379**, 662-671 (2012).

5 Kang, H. *et al.* Chikungunya seroprevalence, force of infection, and prevalence of chronic disability after infection in endemic and epidemic settings: a systematic review, meta-analysis, and modelling study. *Lancet Infect. Dis.* **24**, 488-503 (2024).

6 Wahid, B., Ali, A., Rafique, S. & Idrees, M. Global expansion of chikungunya virus: mapping the 64-year history. *Int. J. Infect. Dis.* **58**, 69-76 (2017).

7 Pialoux, G., Gaüzère, B.-A., Jauréguiberry, S. & Strobel, M. Chikungunya, an epidemic arbovirosis. *Lancet Infect. Dis.* **7**, 319-327 (2007).

8 Rezza, G. *et al.* Infection with chikungunya virus in Italy: an outbreak in a temperate region. *Lancet* **370**, 1840-1846 (2007).

9 Suhrbier, A. Rheumatic manifestations of chikungunya: emerging concepts and interventions. *Nat. Rev. Rheumatol.* **15**, 597-611 (2019).

10 Meyer, A. D. *et al.* Predictability of infectious disease outbreak severity: Chikungunya as a case study. *Sci. Adv.* **11**, eadt5419 (2025).

11 Salje, H. *et al.* How social structures, space, and behaviors shape the spread of infectious diseases using chikungunya as a case study. *Proc. Natl. Acad. Sci. USA.* **113**, 13420-13425 (2016).

12 Economopoulou, A. *et al.* Atypical Chikungunya virus infections: clinical manifestations, mortality and risk factors for severe disease during the

2005–2006 outbreak on Réunion. *Epidemiol. Infect.* **137**, 534-541 (2008).

13 Cauchemez, S. *et al.* Local and regional spread of chikungunya fever in the Americas. *Eurosurveillance* **19**, 20854 (2014).

14 Tsetsarkin, K. A., McGee, C. E. & Higgs, S. Chikungunya virus adaptation to Aedes albopictus mosquitoes does not correlate with acquisition of cholesterol dependence or decreased pH threshold for fusion reaction. *Virol. J.* **8**, 376 (2011).

15 Schwartz, O. & Albert, M. L. Biology and pathogenesis of chikungunya virus. *Nat. Rev. Microbiol.* **8**, 491-500 (2010).

16 Crosby, L. *et al.* Severe manifestations of chikungunya virus in critically ill patients during the 2013–2014 Caribbean outbreak. *Int. J. Infect. Dis.* **48**, 78-80 (2016).

17 Lacerda, M. V. G., Contopoulos-Ioannidis, D., Newman-Lindsay, S., Chow, C. & LaBeaud, A. D. Mother-to-child transmission of Chikungunya virus: A systematic review and meta-analysis. *PLoS Negl. Trop. Dis.* **12**, e0006510 (2018).

18 Rollé, A. *et al.* Severe Sepsis and Septic Shock Associated with Chikungunya Virus Infection, Guadeloupe, 2014. *Emerg. Infect. Dis.* **22**, 891-894 (2016).

19 de Souza, W. M. *et al.* Pathophysiology of chikungunya virus infection associated with fatal outcomes. *Cell Host Microbe* **32**, 606-622 (2024).

20 Couderc, T. *et al.* A Mouse Model for Chikungunya: Young Age and Inefficient Type-I Interferon Signaling Are Risk Factors for Severe Disease. *PLoS Pathog.* **4**, e29 (2008).

21 Vignuzzi, M. & López, C. B. Defective viral genomes are key drivers of the virus–host interaction. *Nat. Microbiol.* **4**, 1075-1087 (2019).

22 Matusali, G. *et al.* Tropism of the Chikungunya Virus. *Viruses* **11**, 175 (2019).

23 Krammer, F. & Palese, P. Advances in the development of influenza virus vaccines. *Nat. Rev. Drug Discov.* **14**, 167-182 (2015).

24 Lum, F.-M. *et al.* Crosstalk between CD64+MHCII+ macrophages and CD4+ T cells drives joint pathology during chikungunya. *EMBO Mol. Med.* **16**,

641-663 (2024).

25 Zhang, R. *et al.* Mxra8 is a receptor for multiple arthritogenic alphaviruses. *Nature* **557**, 570-574 (2018).

26 Zimmerman, O. *et al.* Vertebrate-class-specific binding modes of the alphavirus receptor MXRA8. *Cell* **186**, 4818-4833 (2023).

27 Basore, K. *et al.* Cryo-EM Structure of Chikungunya Virus in Complex with the Mxra8 Receptor. *Cell* **177**, 1725-1737 (2019).

28 Yin, P. *et al.* Chikungunya virus cell-to-cell transmission is mediated by intercellular extensions in vitro and in vivo. *Nat. Microbiol.* **8**, 1653-1667 (2023).

29 Sowinski, S. *et al.* Membrane nanotubes physically connect T cells over long distances presenting a novel route for HIV-1 transmission. *Nat. Cell Biol.* **10**, 211-219 (2008).

30 Roberts, K. L., Manicassamy, B., Lamb, R. A. & Lyles, D. S. Influenza A Virus Uses Intercellular Connections To Spread to Neighboring Cells. *J. Virol.* **89**, 1537-1549 (2015).

31 Pepe, A., Pietropaoli, S., Vos, M., Barba-Spaeth, G. & Zurzolo, C. Tunneling nanotubes provide a route for SARS-CoV-2 spreading. *Sci. Adv.* **8,** eabo7871 (2022).

32 Partidos, C. D. *et al.* Cross-protective immunity against o'nyong-nyong virus afforded by a novel recombinant chikungunya vaccine. *Vaccine* **30**, 4638-4643 (2012).

33 Gardner, J. *et al.* Chikungunya Virus Arthritis in Adult Wild-Type Mice. *J. Virol.* **84**, 8021-8032 (2010).

34 Ordovas-Montanes, J. *et al.* Allergic inflammatory memory in human respiratory epithelial progenitor cells. *Nature* **560**, 649-654 (2018).

35 Ng, L. F. P. *et al.* IL-1β, IL-6, and RANTES as Biomarkers of Chikungunya Severity. *PLoS ONE* **4,** e4261 (2009).

36 Sachs, N. *et al.* Long-term expanding human airway organoids for disease modeling. *EMBO J.* **38,** e100300 (2019).

37 Zhou, J. *et al.* Differentiated human airway organoids to assess infectivity of emerging influenza virus. *Proc. Natl. Acad. Sci. USA.* **115**, 6822-6827 (2018).

38 Deprez, M. *et al.* A Single-Cell Atlas of the Human Healthy Airways. *Am. J. Respir. Crit. Care. Med.* **202**, 1636-1645 (2020).

39 Schoggins, J. W. *et al.* A diverse range of gene products are effectors of the type I interferon antiviral response. *Nature* **472**, 481-485 (2011).

40 Rehwinkel, J. & Gack, M. U. RIG-I-like receptors: their regulation and roles in RNA sensing. *Nat. Rev. Immunol.* **20**, 537-551 (2020).

41 Michlmayr, D. *et al.* Comprehensive innate immune profiling of chikungunya virus infection in pediatric cases. *Mol. Syst. Biol.* **14,** e7862 (2018).

42 Haese, N. N. *et al.* Animal Models of Chikungunya Virus Infection and Disease. *J. Infect. Dis.* **214**, S482-S487 (2016).

43 Herfst, S. *et al.* Airborne Transmission of Influenza A/H5N1 Virus Between Ferrets. *Science* **336**, 1534-1541 (2012).

44 Lowen, A. C., Mubareka, S., Steel, J. & Palese, P. Influenza virus transmission is dependent on relative humidity and temperature. *PLoS Pathog.* **3,** e151 (2007).

45 Leung, N. H. L. Transmissibility and transmission of respiratory viruses. *Nat. Rev. Microbiol.* **19**, 528-545 (2021).

46 Tellier, R., Li, Y., Cowling, B. J. & Tang, J. W. Recognition of aerosol transmission of infectious agents: a commentary. *BMC Infect. Dis.* **19,** 101 (2019).

47 Zhou, J. et al. Human airway and nasal organoids reveal escalating replicative fitness of SARS-CoV-2 emerging variant. *Proc. Natl. Acad. Sci. USA.* **120,** e2300376120 (2023).

Figure legends

Fig. 1 | Human respiratory mucosa permits productive CHIKV infection and transport.

a, Viral genomic loads in nasopharyngeal swabs (NPS) from a cohort of acute patients (n = 26). Patient-23 (Zika-positive) and NC serve as specificity and negative controls, respectively. **b, c,** Viral RNA kinetics in human nasal (b) and airway (c) organoids following apical or basolateral infection measured at 2, 24, 48, 72, and 96 hours post-infection (h.p.i.). Data are presented as mean ± s.d. (n = 3). **d, e,** Infectious titers (PFU) in apical and basolateral supernatants from nasal (d) and airway (e) organoids, demonstrating bidirectional viral release. Data are presented as mean ± s.d. (n = 3). **f,** Representative transmission electron microscopy (TEM) images showing cytopathic vacuoles (CPVs) containing dense virion clusters. **g,** TEM micrographs of nasal epithelium showing tunneling nanotubes (TNTs) acting as conduits for cell-to-cell transmission (top, red arrows indicate the nanotube structure and associated virions) and active viral budding at the plasma membrane (bottom, orange arrow). ****$P <$ 0.0001 (two-way ANOVA with multiple comparisons).

Fig. 2 | CHIKV exhibits broad cellular tropism and dismantles apical tight junctions. a, b, Representative immunofluorescence images of human nasal (a) and airway (b) organoids at 24 h.p.i. Tissues were co-stained for viral E2 antigen (red) and markers for basal (p63), ciliated (β-tubulin), goblet (MUC5AC), and club cells (CC10) (green). Nuclei are counterstained with DAPI (blue) and F-actin with phalloidin (grey). **c, d,** Analysis of tight junction integrity in nasal (c) and airway (d) organoids. Mock tissues display intact, continuous ZO-1 networks (green), whereas infected regions show extensive fragmentation and loss of junctional organization. Scale bars, 20 μm. Images are representative of three independent biological replicates.

Fig. 3 | Single-cell transcriptomics reveals a coordinated pan-epithelial antiviral response. a–c, snRNA-seq workflow (a), UMAP visualization of epithelial clusters (b), and cell type proportions (c) in Mock vs. CHIKV-infected airway organoids. **d,**

Volcano plot highlighting the global upregulation of ISGs (such as *BST2, PTGS2*) across all lineages. **e, f,** KEGG pathway enrichment for Pre-ciliated (e) and Secretory (f) cells. **g,** Box plots of composite Interferon (IFN) and ISG scores; infected cells (CHIKV) show universally elevated antiviral scores. ****$P < 0.0001$, *$P < 0.05$ (two-sided Wilcoxon rank-sum test). **h,** Lineage-specific heatmaps of top DEGs confirming a conserved antiviral signature. **i,** RT-qPCR validation of key proinflammatory cytokines (*IL6, TNF*) and ISGs (*MX1, OAS1*) in nasal organoids. Data were normalized to *GAPDH* levels and are presented as fold change relative to Mock controls. Data are mean ± s.d. (n = 3) (See also Extended Data Fig. 4 for intercellular communication analysis).

Fig. 4 | Intranasal CHIKV infection drives respiratory pathology and systemic dissemination in AG129 mice. a, Schematic of the experimental workflow. **b,** Quantification of viral RNA loads in indicated tissues (Nasal, Lung, Joint, Muscle, Brain, Blood) at 10 days post-infection (d.p.i.). Black bars represent Mock-infected controls, and colored bars represent CHIKV-infected mice. Data are mean ± s.d. derived from n = 3 successfully infected mice (out of n = 5 inoculated animals). Data were analyzed using an unpaired two-tailed *t* test. ***$P < 0.001$, **$P < 0.01$, *$P < 0.05$. **c,** Representative H&E staining of indicated tissues at 10 d.p.i. Respiratory tissues exhibit severe pathology, with arrows indicating: necrosis and sloughing (black), hemorrhage (red) and submucosal infiltration (blue) in nasal turbinates; and atelectasis (black), septal thickening (red) and interstitial infiltration (blue) in lung. Musculoskeletal tissues maintain preserved architecture. Scale bars, 100 μm. **d,** Representative immunofluorescence showing viral dissemination. Tissues were co-stained for MXRA8 (red) and viral E2 antigen (green); nuclei are stained with DAPI (blue). Colocalization confirms systemic spread. Scale bars, 20 μm. **e,** Heat map of qRT-PCR analysis showing relative immune gene expression (fold change). Data were normalized to GAPDH levels and are presented as fold change relative to Mock controls. (n = 3)

Fig. 5 | MXRA8 is the obligate receptor for CHIKV entry in human respiratory epithelia.

a, Representative immunofluorescence images showing endogenous MXRA8 expression (green) in human clinical lung tissue specimens (Patients 1–8). Nuclei are counterstained with DAPI (blue). Scale bar, 10 μm. **b,** Confocal immunofluorescence of MXRA8 expression in Nasal and Airway organoids compared to cell line controls. HEK293T and U2OS cells were included as negative and positive specificity controls, respectively. Scale bar, 20 μm. **c,** Western blot analysis of basal MXRA8 protein levels in organoid lysates and control cell lines. **d,** Immunoblot confirming efficient MXRA8 depletion by shRNA and restoration by the rescue construct in Nasal and Airway organoids. **e,** Quantification of viral replication kinetics following apical infection. Left: Viral genomic RNA copies; Right: Infectious viral titers (PFU/ml). MXRA8 depletion significantly inhibits infection, while complementation restores susceptibility. Data are presented as mean ± s.d. (n = 3). Statistical significance was determined using two-way ANOVA with Šídák's multiple comparisons test. ****P < 0.0001, ***P < 0.001. **f,** Comprehensive model of CHIKV respiratory infection, dissemination, and pathogenesis. **Left: Clinical Evidence**. Analysis of nasopharyngeal swabs from acute patients identifies the upper respiratory tract as a high-load amplification hub (100% positive rate) fueling systemic dissemination. **Middle: Cellular Tropism and Mechanism**. In human respiratory epithelia, CHIKV utilizes the MXRA8 receptor to infect a broad spectrum of lineages, including ciliated, goblet, club, and basal cells. Infection is characterized by bidirectional progeny release facilitating both luminal shedding and systemic entry and efficient intercellular spread via tunneling nanotubes (TNTs). At the molecular level, infection triggers a potent innate immune activation that creates a pathogenic trade-off by suppressing homeostatic tissue repair signaling. **Right: *In vivo* Pathogenesis**. Validation in the AG129 mouse model demonstrates that intranasal challenge leads to productive infection and severe cytopathology in the respiratory tract (necrotizing rhinitis and interstitial pneumonia). Crucially, the respiratory mucosa serves as a functional portal of entry, enabling the virus to breach the barrier, enter the circulation

(viremia), and seed distal musculoskeletal tissues (joints and muscles), initiating systemic inflammatory cascades.

Figures

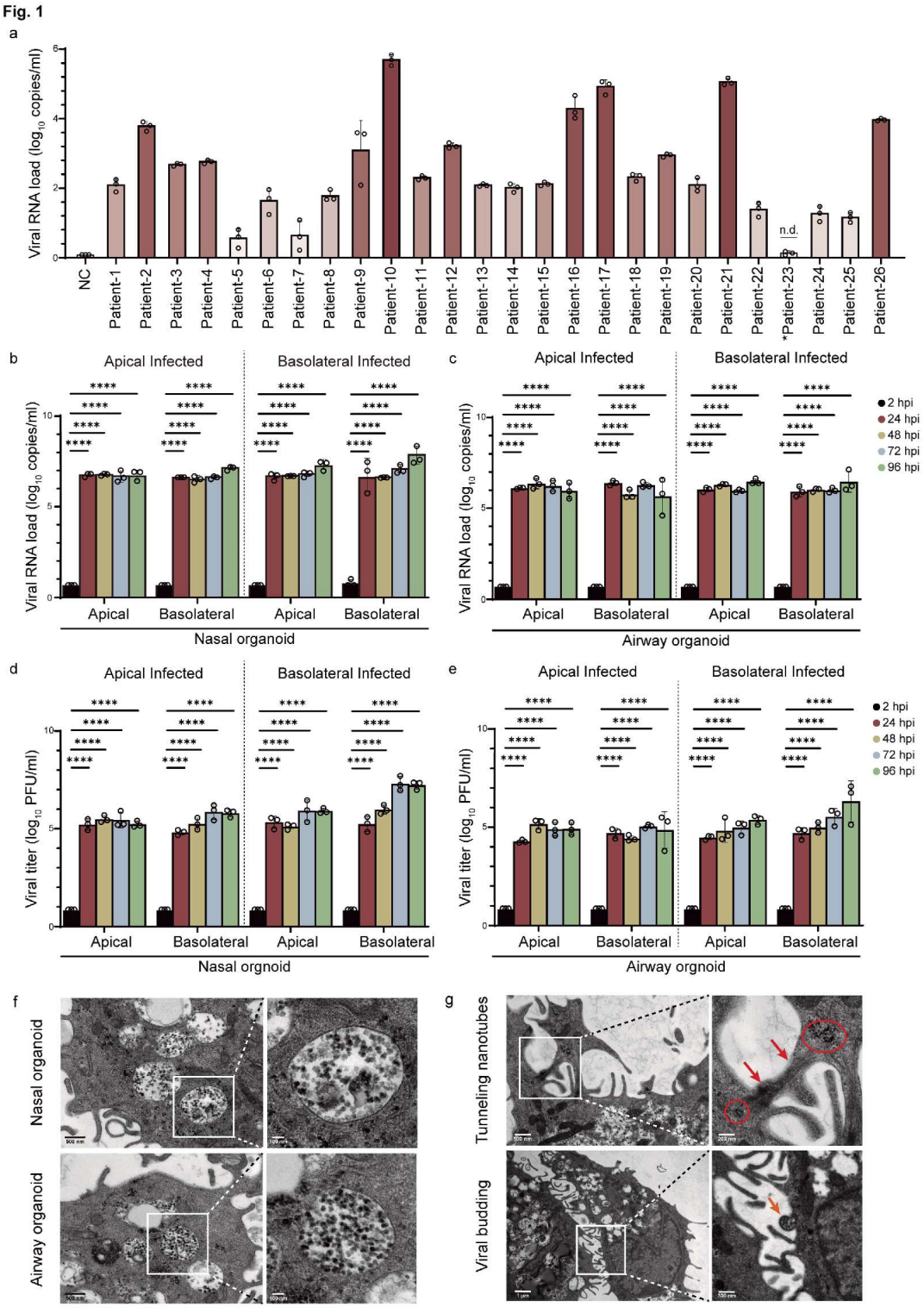


Figure 1

Human respiratory mucosa permits productive CHIKV infection and transport. a, Viral genomic loads in nasopharyngeal swabs (NPS) from a cohort of acute patients (n = 26). Patient-23 (Zika-positive) and NC serve as specificity and negative controls, respectively. b, c, Viral RNA kinetics in human nasal (b) and

airway (c) organoids following apical or basolateral infection measured at 2, 24, 48, 72, and 96 hours post-infection (h.p.i.). Data are presented as mean ± s.d. (n = 3). d, e, Infectious titers (PFU) in apical and basolateral supernatants from nasal (d) and airway (e) organoids, demonstrating bidirectional viral release. Data are presented as mean ± s.d. (n = 3). f, Representative transmission electron microscopy (TEM) images showing cytopathic vacuoles (CPVs) containing dense virion clusters. g, TEM micrographs of nasal epithelium showing tunneling nanotubes (TNTs) acting as conduits for cell-to-cell transmission (top, red arrows indicate the nanotube structure and associated virions) and active viral budding at the plasma membrane (bottom, orange arrow). ****$P < 0.0001$ (two-way ANOVA with multiple comparisons).

Fig. 2

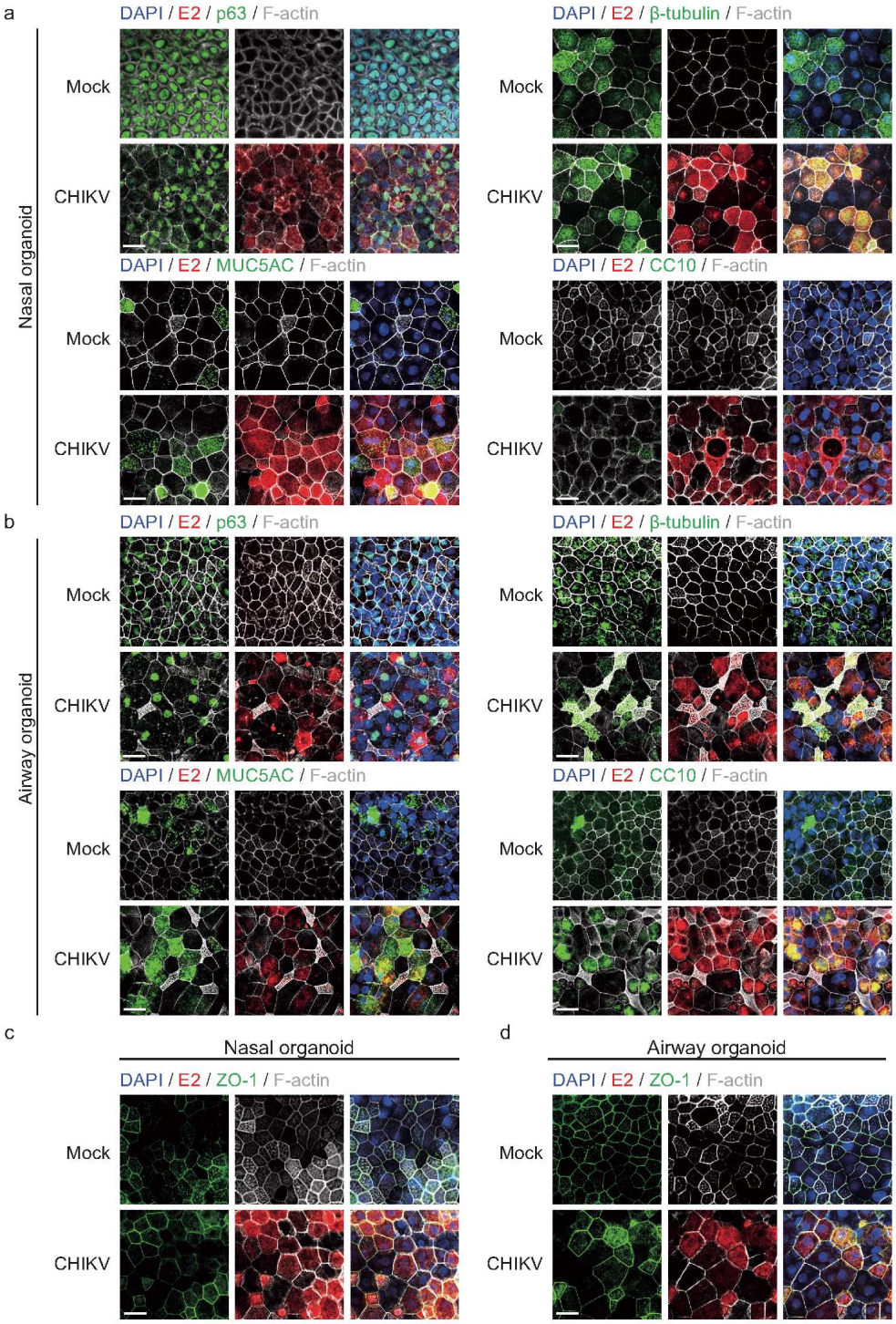


Figure 2

CHIKV exhibits broad cellular tropism and dismantles apical tight junctions. a, b, Representative immunofluorescence images of human nasal (a) and airway (b) organoids at 24 h.p.i. Tissues were co-stained for viral E2 antigen (red) and markers for basal (p63), ciliated (β-tubulin), goblet (MUC5AC), and club cells (CC10) (green). Nuclei are counterstained with DAPI (blue) and F-actin with phalloidin (grey). c, d, Analysis of tight junction integrity in nasal (c) and airway (d) organoids. Mock tissues display intact,

continuous ZO-1 networks (green), whereas infected regions show extensive fragmentation and loss of junctional organization. Scale bars, 20 μm. Images are representative of three independent biological replicates.

Fig. 3

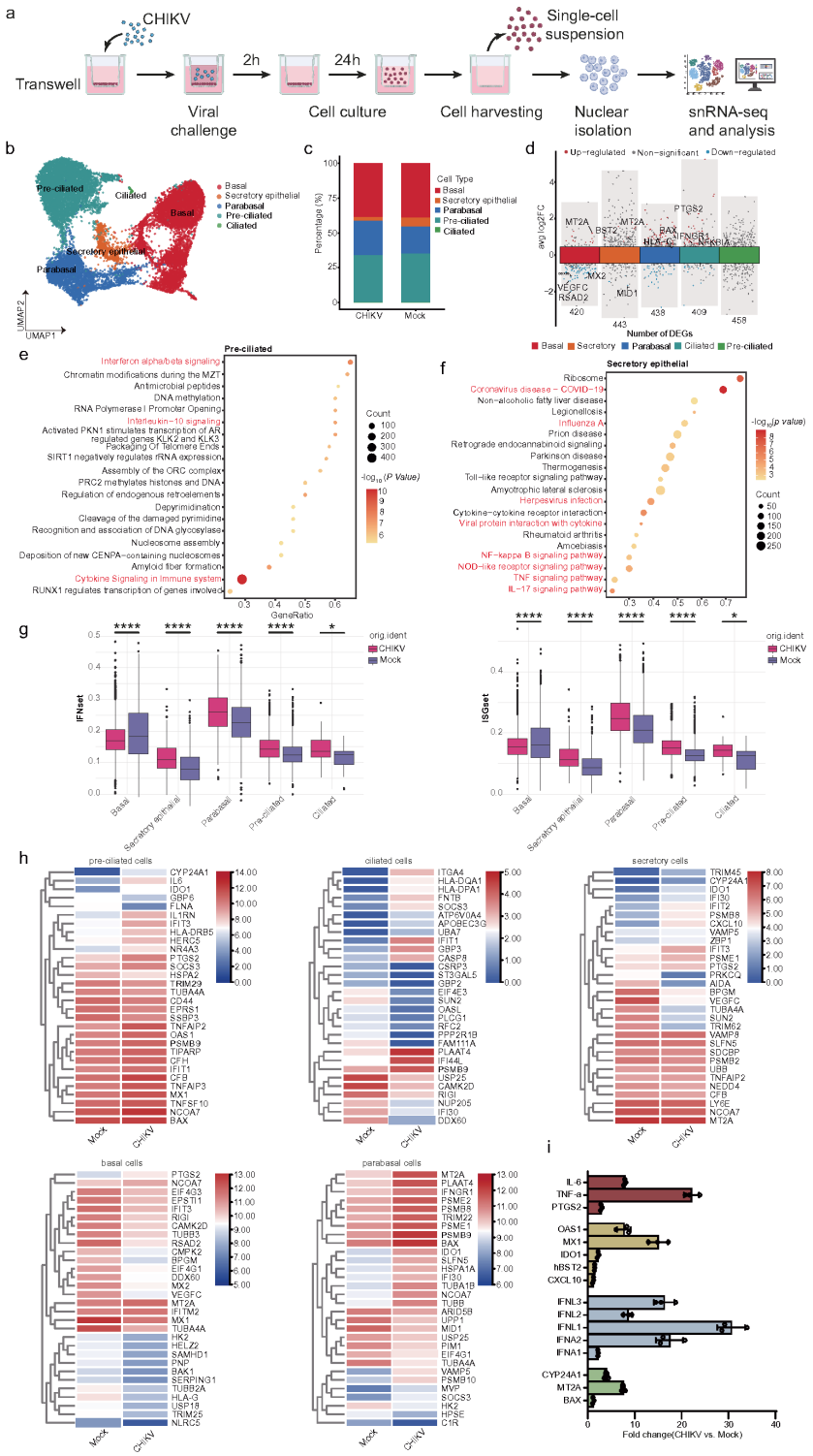


Figure 3

Single-cell transcriptomics reveals a coordinated pan-epithelial antiviral response. a–c, snRNA-seq workflow (a), UMAP visualization of epithelial clusters (b), and cell type proportions (c) in Mock vs.

CHIKV-infected airway organoids. d, Volcano plot highlighting the global upregulation of ISGs (such as BST2, PTGS2) across all lineages. e, f, KEGG pathway enrichment for Pre-ciliated (e) and Secretory (f) cells. g, Box plots of composite Interferon (IFN) and ISG scores; infected cells (CHIKV) show universally elevated antiviral scores. ****P < 0.0001, *P < 0.05 (two-sided Wilcoxon rank-sum test). h, Lineage-specific heatmaps of top DEGs confirming a conserved antiviral signature. i, RT-qPCR validation of key proinflammatory cytokines (IL6, TNF) and ISGs (MX1, OAS1) in nasal organoids. Data were normalized to GAPDH levels and are presented as fold change relative to Mock controls. Data are mean ± s.d. (n = 3) (See also Extended Data Fig. 4 for intercellular communication analysis).

Fig. 4

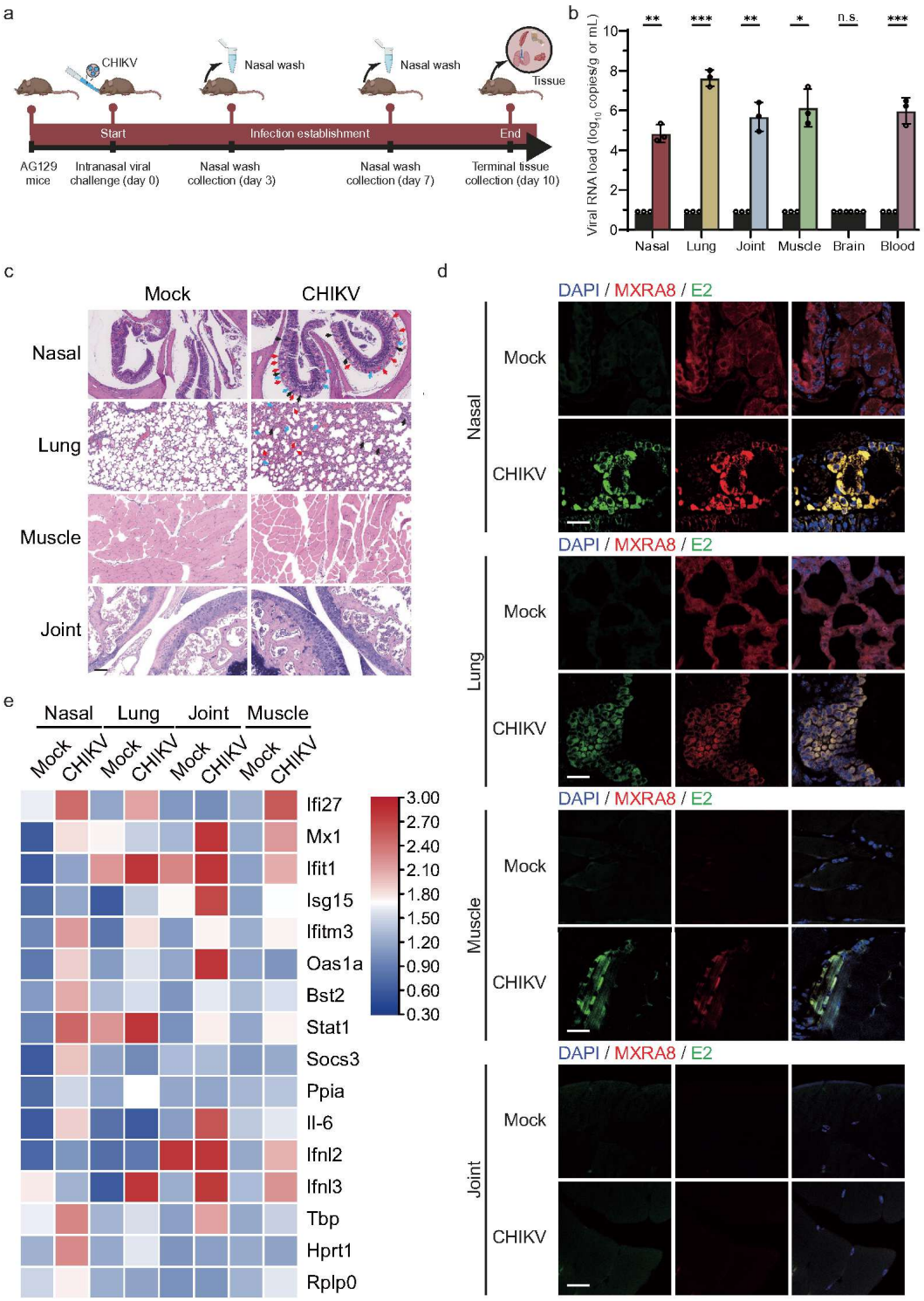


Figure 4

Intranasal CHIKV infection drives respiratory pathology and systemic dissemination in AG129 mice. a, Schematic of the experimental workflow. b, Quantification of viral RNA loads in indicated tissues (Nasal, Lung, Joint, Muscle, Brain, Blood) at 10 days post-infection (d.p.i.). Black bars represent Mock-infected controls, and colored bars represent CHIKV-infected mice. Data are mean ± s.d. derived from n = 3 successfully infected mice (out of n = 5 inoculated animals). Data were analyzed using an unpaired two-

tailed t test. ***P < 0.001, **P < 0.01, *P < 0.05. c, Representative H&E staining of indicated tissues at 10 d.p.i. Respiratory tissues exhibit severe pathology, with arrows indicating: necrosis and sloughing (black), hemorrhage (red) and submucosal infiltration (blue) in nasal turbinates; and atelectasis (black), septal thickening (red) and interstitial infiltration (blue) in lung. Musculoskeletal tissues maintain preserved architecture. Scale bars, 100 μm. d, Representative immunofluorescence showing viral dissemination. Tissues were co-stained for MXRA8 (red) and viral E2 antigen (green); nuclei are stained with DAPI (blue). Colocalization confirms systemic spread. Scale bars, 20 μm. e, Heat map of qRT-PCR analysis showing relative immune gene expression (fold change). Data were normalized to GAPDH levels and are presented as fold change relative to Mock controls. (n = 3)

Fig. 5

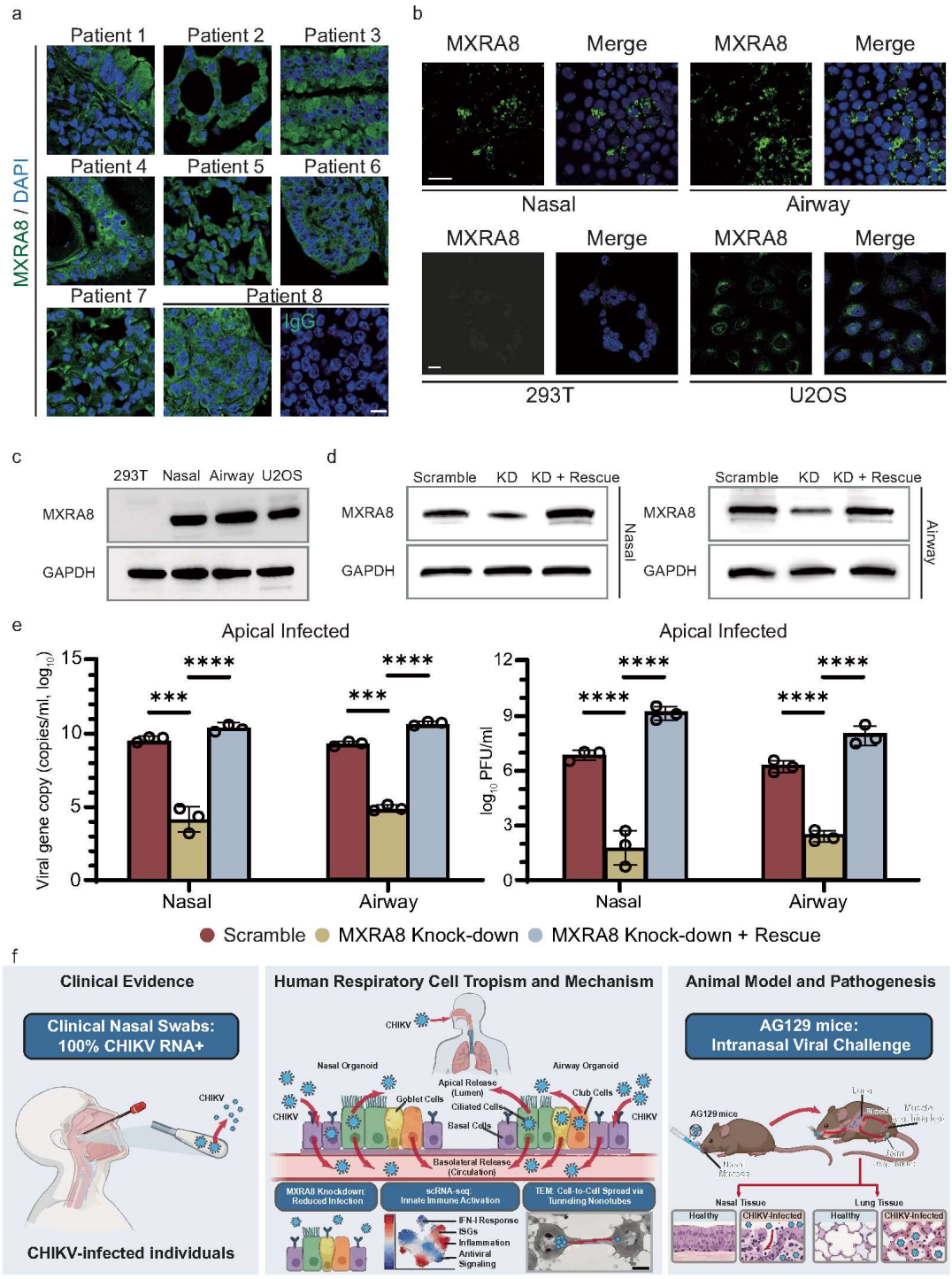


Figure 5

MXRA8 is the obligate receptor for CHIKV entry in human respiratory epithelia. a, Representative immunofluorescence images showing endogenous MXRA8 expression (green) in human clinical lung tissue specimens (Patients 1–8). Nuclei are counterstained with DAPI (blue). Scale bar, 10 μm. b, Confocal immunofluorescence of MXRA8 expression in Nasal and Airway organoids compared to cell line controls. HEK293T and U2OS cells were included as negative and positive specificity controls,

respectively. Scale bar, 20 μm. c, Western blot analysis of basal MXRA8 protein levels in organoid lysates and control cell lines. d, Immunoblot confirming efficient MXRA8 depletion by shRNA and restoration by the rescue construct in Nasal and Airway organoids. e, Quantification of viral replication kinetics following apical infection. Left: Viral genomic RNA copies; Right: Infectious viral titers (PFU/ml). MXRA8 depletion significantly inhibits infection, while complementation restores susceptibility. Data are presented as mean ± s.d. (n = 3). Statistical significance was determined using two-way ANOVA with Šídák's multiple comparisons test. ****P < 0.0001, ***P < 0.001. f, Comprehensive model of CHIKV respiratory infection, dissemination, and pathogenesis. Left: Clinical Evidence. Analysis of nasopharyngeal swabs from acute patients identifies the upper respiratory tract as a high-load amplification hub (100% positive rate) fueling systemic dissemination. Middle: Cellular Tropism and Mechanism. In human respiratory epithelia, CHIKV utilizes the MXRA8 receptor to infect a broad spectrum of lineages, including ciliated, goblet, club, and basal cells. Infection is characterized by bidirectional progeny release facilitating both luminal shedding and systemic entry and efficient intercellular spread via tunneling nanotubes (TNTs). At the molecular level, infection triggers a potent innate immune activation that creates a pathogenic trade-off by suppressing homeostatic tissue repair signaling. Right: In vivo Pathogenesis. Validation in the AG129 mouse model demonstrates that intranasal challenge leads to productive infection and severe cytopathology in the respiratory tract (necrotizing rhinitis and interstitial pneumonia). Crucially, the respiratory mucosa serves as a functional portal of entry, enabling the virus to breach the barrier, enter the circulation (viremia), and seed distal musculoskeletal tissues (joints and muscles), initiating systemic inflammatory cascades.

Supplementary Files

This is a list of supplementary files associated with this preprint. Click to download.

- SupplementaryTable1.pdf
- SupplementaryTable3.pdf
- ExtendedDataFigure1.pdf
- ExtendedDataFigure5.pdf
- SupplementaryTable2.pdf
- ExtendedDataFigure4.pdf
- ExtendedDataFigure2.pdf
- ExtendedDataFigure3.pdf